Dollinger, Christoph ; Balaresque, Nicholas ; Sorg, Michael ; Fischer, Andreas

IR thermographic visualization of flow separation in applications with low thermal contrast

Take down policy
If you believe that this document or any material on this site infringes copyright, please contact
publizieren@suub.uni-bremen.de with full details and we will remove access to the material.

IR thermographic visualization of flow separation in applications with low thermal contrast

C. Dollinger [a,*], N. Balaresque [b], M. Sorg [a], A. Fischer [a]

[a] University of Bremen, Bremen Institute for Metrology, Automation and Quality Science, Linzer Str. 13, 28359 Bremen, Germany
[b] Deutsche WindGuard Engineering GmbH, Überseering 7, 27580 Bremerhaven, Germany

HIGHLIGHTS

- Two methods for a thermographic visualization of separated flow are proposed.
- Visualization without explicit additional heating of the measured object.
- Validation with wind tunnel experiments on a circular cylinder and a NACA 63_3-618.
- The underlying approaches are based on a thermographic time series analyses.
- Both methods enable a fast and noninvasive visualization of separated flow.

1. Introduction

Flow separation on an rotor blade of a wind turbine is an undesirable phenomenon as it results in a sudden decrease in lift and an increase in drag [31,12]. Furthermore, the resulting periodic shedding of the flow leads to unsteady structural loads and to vibrations [26]. On rotor blades for wind turbines, flow separation is an often present flow state especially near the root of the rotor blade [13]. Beside the negatively affected overall performance, the unsteady loads due to flow separation reduce the lifetime of the wind turbine and cause flow and vibration induced acoustic emissions, which complicate the siting and lower the social acceptance. In order to study the effects and resulting mechanisms close to the real application, a measurement of the flow separation phenomena on rotating wind turbines is demanded.

State-of-the-art methods for determining the location of a separated flow region at wind turbines in operation involve tufts [33], stall flags [3] or oil solutions [21]. However, the placement and precise positioning of the means is a time consuming and costly operation for these methods. Moreover they are invasive and, thus, have an influence on the boundary layer itself, resulting in an affected downstream flow. Since invasive measurement techniques are unsatisfactory and the observation of the rotor blade

* Corresponding author.
E-mail address: c.dollinger@bimaq.de (C. Dollinger).

under real conditions is a key task in validating the desired performance of the rotor blade, a novel non-invasive measurement technique is needed that requires no preparation of the rotor blade. For this purpose, the capability of flow separation visualization using infrared (IR) thermographic flow visualization is investigated.

A thermographic measurement has the potential to deliver the similar information as the invasive methods, but is non-invasive, reaction-less and faster (no preparation of the rotor blade). As state of the art, the IR thermographic flow visualization is a known technique for the visualization of different flow regimes in the boundary layer. Based on a temperature difference between the object and the incoming flow, changes in the boundary layer can be distinguished by measuring the surface temperature with a thermographic camera. The surface temperature depends on the local heat transfer between the object and the flow, which is proportional to the skin friction in different flow regimes [27,19,10]. Wind tunnel applications for this method are the localization of the laminar-turbulent transition [9], the identification of laminar separation bubbles [23] or the visualization of a turbulent separation [10]. For a sufficient contrast in the thermographic images, the observed object is usually externally [2] or internally [20] heated or cooled. Additionally an insulation against the internal thermal conductivity of the object enhances the contrast and improves the thermodynamic response behavior [32]. The successful transfer of these techniques from the laboratory to the area of operation is reported in particular regarding the detection of the laminar-turbulent transition, e.g., for in-flight experiments on aircraft wings [4] as well as for measurements on rotating helicopter blades [15,18] and on rotating wind turbine blades [7]. Recently, the automated detection of the laminar transition is proposed by Crawford et al. [5] and by Joseph et al. [17] in order to gain also quantitative information, e.g., within long lasting wind tunnel campaigns. Furthermore, an image processing is presented in Raffel et al. [28] that addresses the thermodynamic response of the object surface for enabling the measurement of fast position changes of the laminar-turbulent transition.

For the thermographic detection of the laminar-turbulent transition, heating power levels between several hundred [17] up to a few thousand [18,32] W m^{-2} are reported. This results in a temperature difference between the tested object and the flow of a few Kelvin. Gardner et al. [8] recently described a method for the dynamic and static stall detection with thermographic measurements by the evaluation of the spatial standard deviation from a high-frequency sampled series (107 Hz) of consecutive differential thermography images. With the described method, spatial resolved information of the flow conditions can be obtained at temperature differences between the measurement object and the flow in the order of 10 Kelvin. However, on wind turbines in operation, there is no feasibility for a uniformly active heating of the rotor blade and a thermal insulation of the surface of the rotor

blade cannot be installed. The available thermal contrast between the rotor blade and the incoming flow is only based on the absorbed solar radiation, which can be estimates to 175 W m^{-2} during the summer (cf. Section 2). The resulting relatively low temperature difference can lead to a poor image contrast, which makes it difficult to visualize different flow regimes [6]. Under sufficiently sunny conditions it is possible to detect a satisfactory difference between laminar and turbulent flow regimes and to localize the transition between both regimes [6]. The ability of the sun for heating the observed object has also been proven by Richter and Schülein [30]. However, flow separation on wind turbine rotor blades is not detectable. As a result, the contrast of the thermographic flow visualization has to be increased with respect to the flow separation phenomena for enabling the visualization of separated flow.

For this reason, a novel thermographic measurement approach is demonstrated, where the small temperature fluctuations within a time series of thermographic images are evaluated. This measurement approach, which is based on time-resolved IR thermography, determines temporal temperature variations in order to allow the identification of separated flow regions even at conditions with low thermal contrast. For validating the measurement approach, wind tunnel measurements were conducted on a non-heated, non-isolated circular cylinder in crossflow as well as on a 6 digit NACA-airfoil. First the measurement approach is explained in Section 2. After the subsequent description of the experimental setup in Section 3, the thermographic measurement results are presented in Section 4, which are validated by mean surface pressure measurements, oil flow visualization and acoustic measurements in the boundary layer for the cylinder measurements. The article closes with a summary and outlook in Section 5.

2. Measurement approach

With measurements on a wind turbine in operation in mind, the measurement approach deals with the enhancement of the contrast between turbulent and separated flow to distinguish these regions without an additional heating or coating of the rotor blade. The approach includes the acquisition and the evaluation of a time series instead of a single thermographic image. By that, small temperature differences in terms of temperature fluctuations in time are visualized by a previously executed image processing. The underlying hypothesis of the measurement approach is that regions of laminar, turbulent and separated flow can by distinguished by differences of the measured temperature fluctuations.

Fig. 1 illustrates the different flow regions in the boundary layer around a circular cylinder in the supercritical regime above the critical Reynolds number $\mathrm{Re_{crit}} = 4.0 \times 10^5$ [31]. The angular positions are specified by the angle ϕ around the cylinder, starting at
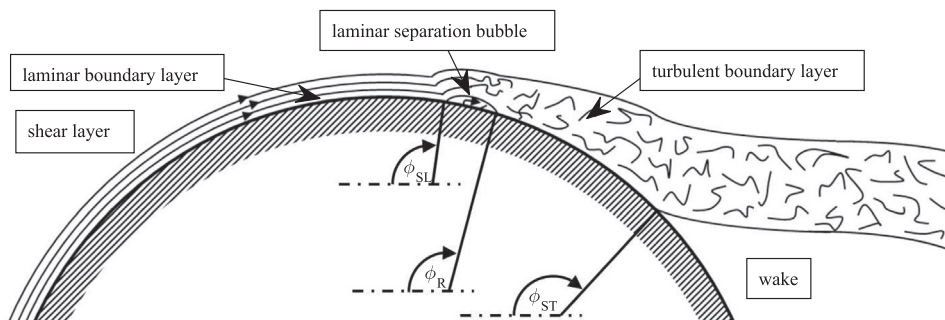

Fig. 1. Schematic sketch of the different flow regions in the boundary layer around a circular cylinder in the supercritical regime above the critical Reynolds number $\mathrm{Re_{crit}} = 4.0 \times 10^5$ [31], with the angular positions for a laminar separation ϕ_{SL}, a reattachment of the flow ϕ_R and a turbulent separation ϕ_{ST}.

the leading edge with 0°. In the region of the laminar flow, the conditions in the boundary layer are very stable and the streamlines are ordered regularly within the boundary layer, cf. Fig. 1. In the supercritical regime, the transition between laminar and turbulent flow appears over a laminar separation bubble with the angular dimension $\phi_R - \phi_{SL}$. According to Ricci and Montelpare [29] a lowered heat flux due to the isolating effect of the self contained laminar separation bubble is characteristic for this region. In contrast to a region of laminar flow, the flow in a turbulent boundary layer is irregular and the stream direction oscillates with a time-dependent transverse component [16]. This condition goes along with a significant increase in skin friction and, thus, an increase in heat flux between the flow and the surface. For a high positive pressure gradient the boundary layer finally separates from the cylinder in a turbulent separation at the angle ϕ_{ST} [31]. Behind the position of the separation downstream, the skin friction and heat flux does not change anymore and is nearly constant [19]. As a result, the different boundary layer flow states lead to different heat flux conditions between the cylinder surface and the flow. In order to distinguish the different temperature fluctuations on the surface due to the boundary layer state, an evaluation of a temperature time series by means of a standard deviation and a Fourier analysis for selected Fourier coefficients is investigated.

Regarding future measurements on the wind turbine in operation, there are two important constraints that are already addressed in the preliminary wind tunnel experiments. One constraint is due to the missing feasibility of an additional heating technique. Therefore the available thermal contrast between the rotor blade and the incoming flow is only based on the solar radiation that is absorbed by the rotor blade. The following simplified model is used to estimate the maximum intensity of the absorbed radiation. For further particulars on the calculations used in the model see Muneer [25] and Meinel [22]. The model is based on the assumption, that the overall absorption coefficient α of the rotor blade is 0.25 (measured on a weathered surface of a rotor blade) and the rotor blade is aligned at an angle of 90° with respect to the ground. The estimation is valid for the location of Bremen (latitude = 53.08° and longitude = 8.80°) for the 21st June, which represents the longest day in the year with the highest angle of the sun above the horizon. Fig. 2a shows the calculated angles of the sun above the ground and above the blade surface over the day in the time frame UTC + 1. The different resulting radiation intensities on the ground and on the rotor blade are depicted in Fig. 2b over the daytime together with the solar constant. The solar radiation that reaches the atmosphere (the solar constant) is reduced on the way through the atmosphere by absorption and scattering. The intensity on the ground depends on the distance through the atmosphere (depending on the altitude of the sun) and the angle of incidence on the observed surface. The angle of incidence is the reason why the radiation on the rotor blade differs from the radiation on the ground. Finally only a fraction of the radiation is absorbed by the surface of the rotor blade, which can be described by the absorption coefficient α. Without having found a suitable reference for the overall absorption coefficient of polyurethane as the top coat material of a rotor blade, the overall absorption coefficient was determined by measuring a weathered rotor blade and results in $\alpha = 0.25$. The absorbed radiation intensity is also shown in Fig. 2b. As a result, the maximal absorbed radiation amounts to 175 W m^{-2}. Due to any kind of clouds, the value is expected to be even lower. In contrast to the reported heating power levels between several hundreds and a few thousand W m^{-2} in thermographic flow analyses up to now [17,18,32], the expected levels on a wind turbine in operation are, even under the assumed optimal conditions, at least one order of magnitude lower. In order to consider this constraint in the experiments, no additional heating or cooling is installed at the measurement
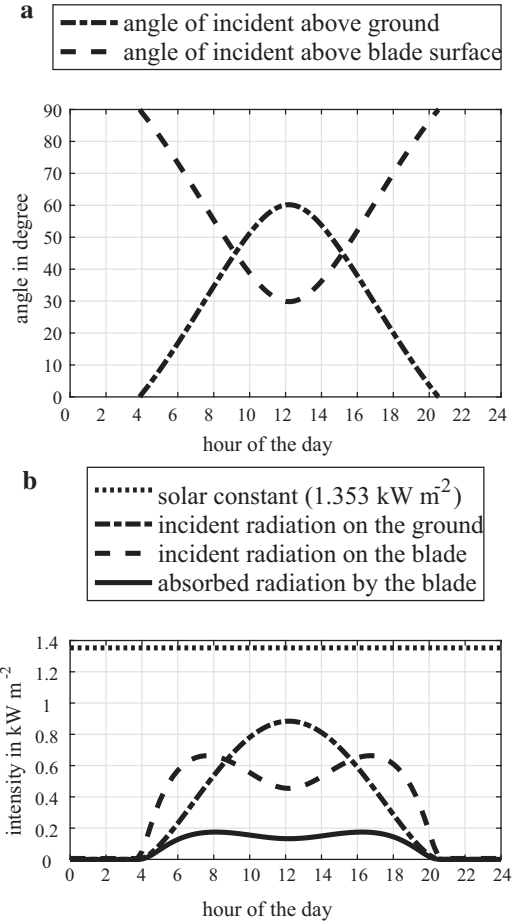

Fig. 2. Estimation of the absorbed solar radiation by the rotor blade surface for the location of Bremen, Germany on the 21st of June. **a** The angles of incident for the ground and the rotor blade **b** The resulting radiation intensities reduced by effects of the atmosphere and the incident angle.

objects. The only source of additional heating energy is due to the layout of the wind tunnel as a closed-return type and the continuously heating up of the flow during operation due to friction in the wind tunnel system. All of the presented experiments are conducted at a wind speed of 50 m s^{-1}. For this wind speed the average temperature rise in the test section is of the magnitude of 0.11 K min^{-1}. The temperature in the test section is calculated based on PT100 resistance thermometer temperature measurements in the wind tunnel settling chamber.

The second challenge regarding the measurements on wind turbines in operation is based on the rotation of the rotor and the resulting movement of the rotor blade with typical tip speeds between 80 and 90 m s^{-1} [11,14]. In order to capture a time series of the same surface area, the blade either has to be tracked and followed by the optical system (for instance with a rotating mirror as in Heineck et al. [15]) or every single image has to be taken at the same rotor position while the wind conditions are assumed to be constant. Here it is intended to concentrate on the possibility to work with the limited information from an IR camera with a low frame rate, i.e., only a few images can be captured per revolution. This is mainly due to the requirements of low complexity and relatively low costs of the system to develop. This constraint results in a sampling frequency of $\frac{1}{6}$ Hz for 10 rpm of the rotor, as the blade passes every 6 s the camera field of view. Assuming that all rotor blades are similar and face the same conditions, the sampling frequency can be raised to $\frac{1}{2}$ Hz by acquiring an image every time one

of the three blades passes the camera field of view. Regarding the acquisition of temperature fluctuations, this means a distinct undersampling of the signal. In order to consider this constraint, the sampling frequency of the thermographic images in the wind tunnel tests is also set to $\frac{1}{2}$ Hz.

3. Experimental setup

In order to demonstrate the feasibility and to investigate the potential of the measurement approach, wind tunnel experiments are performed. The measurements are conducted at the Deutsche WindGuard aero-acoustic wind tunnel in Bremerhaven, Germany, which is described in Section 3.1. The first measurement setup with a circular cylinder is explained in Section 3.2. The setup is equipped with several reference measurement techniques for verifying the novel measurement approach. The second measurement object is a NACA-airfoil, which is described in Section 3.3. Finally, the setup and the image processing for the time-resolved IR thermography is presented in Section 3.4. Note that no external heating, except the waste heat of the wind tunnel due to operation, is applied during the measurements in all of the experiments. An initial temperature difference between the rotor blade surface and the incoming flow is still required for the novel measurement approach, but the necessary magnitude of the temperature difference is reduced.

3.1. Aero-acoustic wind tunnel

The aero-acoustic wind tunnel in Bremerhaven is a closed-return type in which laminar flows (turbulence intensity < 0.3%) at wind speeds of up to 100 m s^{-1} and chord-Reynolds numbers of up to 6.0×10^6 can be achieved. The wind tunnel can be operated either with an open or a closed test section and is designed for acoustic and aerodynamic research. The closed test section allows testing of up to 0.9 m chord models, therefore wind turbine airfoil segments (2D) as well as winglets can be tested at or close to a 1:1 scale. The aerodynamic models are mounted vertically between two turntables. The lift force can be measured directly through force measurements on the turntables and indirectly through pressure measurements both on the wind tunnel sidewalls and on the model surface. A combination of a 6 component force balance attached to the base turntable and a 2 component force balance attached to the upper turntable allows a direct measurement of the total wind forces acting on the model, respectively.

3.2. Cylinder model

In order to evaluate the feasibility of distinguishable flow regions due to different temperature fluctuations, measurements on a circular cylinder with a diameter of 160 mm in the supercritical regime at Re 5.2×10^5 were performed. This corresponds to a wind speed in the wind tunnel test section of 50 m s^{-1}. The measurements were accompanied by oil flow visualizations, acoustic measurements and surface pressure measurements. The results of these additional measurements are consulted to verify the position of the different flow regions. A design-drawing of the circular cylinder model used in the wind tunnel experiments is shown in Fig. 3. The manufactured cylinder is mounted vertically between the two turntables of the test section. The cylinder with 73 equally spaced pressure taps and a flush-mounted microphone is made of polyoxymethylene (POM). This material allows a high quality machining and, due to its optical and thermal properties, is appropriate for thermal imaging without the need of an additional surface preparation. In comparison with metallic models, POM provides a higher emissivity as well as a lower heat capacity and
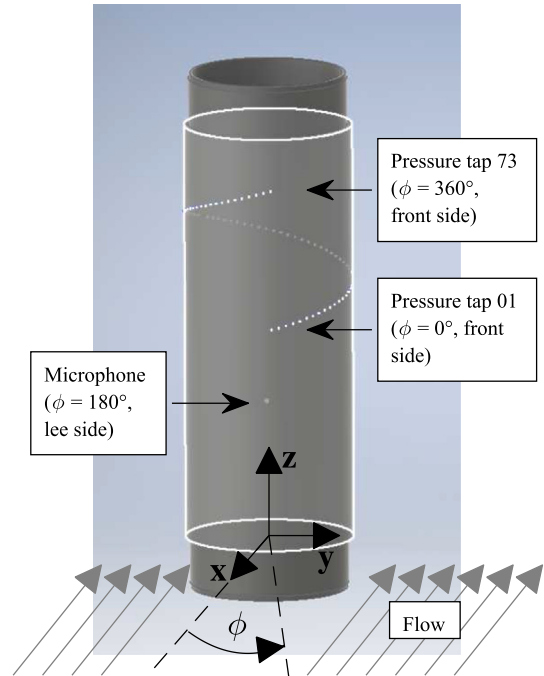

Fig. 3. Design-drawing of the circular cylinder with 73 equally spaced pressure taps and a flush mounted microphone.

heat conduction. Furthermore the properties are comparable to that of a rotor blade.

The cylinder consists of 3 parts: The center part, in which the pressure taps and the microphone are located, is manufactured from black POM. The uninstrumented lower and upper sections are manufactured from white POM to provide more flexibility regarding the oil flow visualization and the pigment choice. The surface roughness in the direction of flow is about Ra = 0.44 µm and Rq = 0.57 µm, respectively.

3.2.1. Surface pressure measurements

Surface pressure measurements are performed simultaneously to the thermographic measurements, using independently connected high range piezo pressure sensors for each port. The sensors measure in differential mode and the pressure range is from 0 to ±500 mbar at an output voltage from 0.5 to 4.5 V. The manufacturer spezifies a total accuracy of ±0.5% of the output span ±0.02V ≙ ± 5 mbar. The pressure sensors are connected to the 73 pressure taps in the surface of the circular cylinder. The pressure taps have an inner diameter of 0.3 mm, are equally spaced in 5° steps in azimuthal direction and the center line is inclined by 15° to avoid disturbances between the different pressure taps due to turbulence wedges caused by imperfections of the mounting. Tests showed that none of the pressure taps cause a premature laminar-turbulent transition. The two pressure taps located at $\phi = 0°$ and 360° are roughly 135 mm apart from each other in spanwise direction, cf. Fig. 3.

3.2.2. Oil flow visualization

A daylight fluorescent pigment is used together with silicone oil for flow visualization. The images are acquired with the wind tunnel in operation. Due to the fact that the separation location is extremely sensitive to surface roughness and geometrical steps [1], great care was taken to use as little oil-pigment solution as possible. As soon as the oil layer gets thicker and accumulation occurs (i.e., in a laminar separation bubble) the turbulent separation point is shifted noticeably. A series of optical images is taken

every 30 s with a digital single-lens reflex (DSLR) camera in order to document the settling of the oil flow pattern. This also allows the identification of local accumulations that artificially modify the flow field and the selection of an appropriate image.

3.2.3. Acoustic measurements

The use of a microphone on the lee side of the cylinder is intended for an acoustic analysis of the vortex shedding with a rotation of the cylinder. The applied microphone is an electret condenser microphone with a sensitivity of -43 dB $\pm$ 3 dB @ 94 dB sound pressure level. With a diameter of about 2.55 mm and a height of about 2.59 mm, the microphone is small enough to be flush-mounted in the cylinder without influencing the boundary layer in terms of premature laminar-turbulent transition.

3.3. NACA 63_3-618 airfoil

For the measurements on an airfoil, that is also used for wind turbines, a 6 digit NACA 63_3-618 airfoil with a chord length of 600 mm is used. The measurements were performed at a chord Reynolds number of Re 2.0×10^6, which corresponds to a wind speed in the wind tunnel test section of 50 m s^{-1}. Hence, the wind speed for the measurement on the circular cylinder and on the airfoil is the same. The airfoil has a maximum thickness of 18 % at 34.7 % chord and the maximum camber is 3.3 % at 50 % chord. Geometrical information for the two dimensional profile of the airfoil is shown in Fig. 4. The wind tunnel model of the airfoil is made out of glass-fiber reinforced plastic (GFRP) with a polyurethane top coat as it is typical for rotor blades of wind turbines. The surface roughness of the airfoil in the direction of flow is about Ra = 0.30 μm and Rq = 0.47 μm, respectively.

3.4. IR thermography and image processing

The thermographic measurements are accomplished with two different cameras, both manufactured by the company *InfraTec*. A photo of the setup is shown in Fig. 5. For a general overview image of the cylinder in the test section, an uncooled microbolometer camera (model *VarioCAM hr head*) with a noise equivalent temperature difference NETD of < 30 mK @ 30 °C is used. The camera has a format of 640×480 pixels and the dynamic range is 16 bit. The spectral range of the IR camera is between 7.5 and 14 μm. The access to the wind tunnel section is provided by a ZnSe (zinc selenide) window with a transmission in the camera spectral range of higher than 70 %, cf. Fig. 6. As the overview images are intended to deliver information about the overall spanwise flow and no subsequent image processing is performed, this microbolometer camera with a rolling shutter is sufficient for this task. For the measurements of the dynamic behavior of the temperature fluctuations, a camera with a global shutter (snap-shot detector) is used. The acquisition of the detailed image series of the cylinder is realized with a cooled InSb focal plane array with a detector format of 640×512 pixels (model *ImageIR 8300*). The pixel size amounts to 15 μm. Full-frame resolution images can be acquired with up

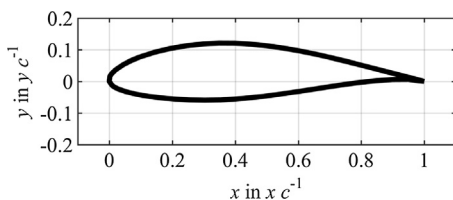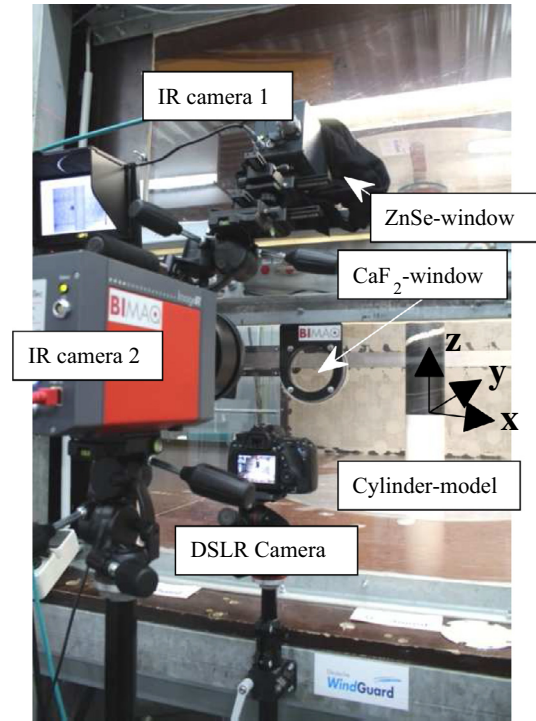**Fig. 5.** Experimental setup with mounted cylinder in the test section of the aeroacoustic wind tunnel and a digital single-lens reflex (DSLR) camera as well as 2 IR thermographic cameras observing it.
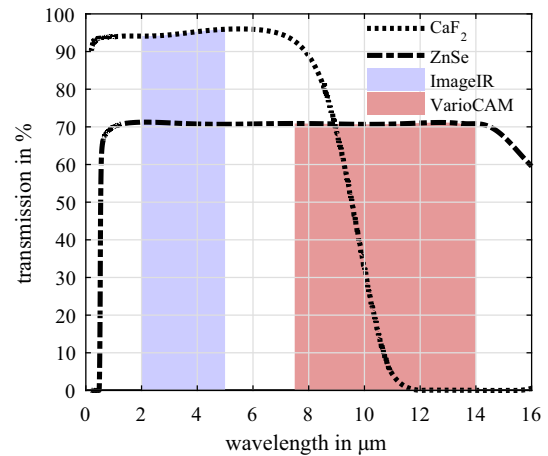

Fig. 6. Transmission of the IR-windows and spectral range of the used IR thermographic cameras.

to 100 Hz. The camera is sensitive between 2 and 5 μm and the NETD for this camera is less than 25 mK @ 30 °C. The dynamic range is 14 bit and the integration time for the acquisition of an image can be set between 1 and 20,000 μs. The camera is equipped with a 100 mm telephoto lens with an angular aperture of $5.5° \times 4.4°$. This results in an instantaneous field of view of 0.15 mrad for the given detector size. With a viewing distance of 1.75 m follows that 0.26 mm in the frame of the measurement object are represented by one pixel. This camera observes the test section through a CaF$_2$ (calcium fluoride) window with more than 90 % transmission between 2 and 5 μm, cf. Fig. 6.

The IR thermographic images are acquired with the camera software development kit (SDK) from the camera manufacturer. It provides an interface to MATLAB, which is used for the subse-

Fig. 4. Geometrical information for the two dimensional profile of the NACA 63_3-618 airfoil.

quent processing of the image series. For an accurate assignment of each pixel to the corresponding position on the surface of the observed object, the direction of view of the camera and the angle of aperture of the telephoto lens in combination with the object geometry are taken into account. As a result, image deformations due to the object geometry and a viewing direction that is not normal to the flow are corrected. Note that changes in emissivity due to the surface curvature and the viewing angle are not taken into account.

The spatial dimension of each image within the series is $M \times N$ pixel and $J = 30$ images are acquired. Typical values for M and N are the size of the detector, i.e., in this case 512×640 pixels, but there is nothing wrong with reducing the region of interest, e.g., to reduce computation time. The evaluation of the fluctuations within the thermographic image series is performed with two different methods. The first method uses the standard deviation σ_{mn} of each temperature series $T_{mn}[j], j = 1, \ldots, J$, at the pixel row number $m = 1, \ldots, M$ and the pixel column number $n = 1, \ldots, N$ of the thermographic image series

$$\sigma_{mn} = \sqrt{\frac{1}{J-1} \sum_{j=1}^{J} \left(T_{mn}[j] - \overline{T}_{mn}\right)^2}. \tag{1}$$

The symbol $\overline{T}_{mn}$ denotes the arithmetic mean of each temperature series within the images, i.e., $\overline{T}_{mn} = \frac{1}{J} \sum_{j=1}^{J} T_{mn}[j]$.

The second method for the evaluation is based on a Fourier analysis of the temperature series of each pixel. The Fourier coefficients of the discrete Fourier transform (DFT) $\widehat{T}_{mn}$ for the temperature series $T_{mn}[j]$ are given by

$$\widehat{T}_{mn}[k] = \frac{1}{J} \sum_{j=0}^{J-1} e^{-2\pi i \frac{jk}{J}} T_{mn}[j] \quad , k = 0, 1, \ldots, J-1. \tag{2}$$

Here, the two Fourier coefficients $k = 1$ and $k = 2$ are selected due to the highest dynamic ranges within the coefficients and the expected low frequencies of the fluctuations. The evaluation quantity is the mean value of two times the absolute value of both Fourier coefficients that corresponds to the average amplitude of the respective temperature fluctuation: $P_{mn} = |\widehat{T}_{mn}[1]| + |\widehat{T}_{mn}[2]|$. The different methods for the evaluation of the image series are compared to each other in terms of significance and contrast-to-noise ratio (CNR) in Section 4.1.

4. Measurement results

The thermographic measurement results are presented in Section 4.1. In order to determine the position of the different flow regions, a surface pressure measurement as well as an oil flow visualization are discussed first. In addition an acoustic measurement in the boundary layer of the circular cylinder is presented for visualizing the different conditions in the different flow regions in terms of pressure fluctuations. Furthermore, the thermographic measurements on the 6 digit NACA-airfoil are discussed in Section 4.2. For all of the presented results, the main flow direction is from left to right.

4.1. Circular cylinder

The result of the surface pressure measurement for the cylinder at Re 5.2×10^5 is given in Fig. 7. The result is overlaid with pressure distributions of different flow ranges from literature, which can be found in Morkovin [24]. The measured pressure distribution in combination with a measured drag coefficient $C_D \approx 0.3$ (determined with the force balance in the wind tunnel) allows to assign the present flow state to the supercritical range. Note that the pressure taps are located with an azimuthal distance of $5°$ which limits the resolution for determining characteristic positions. The measured pressure distribution indicates a laminar separation at the angle $\phi_{SL} \approx 100 - 105°$, which is identifiable by the small kink in the distribution, and a turbulent separation at the angle $\phi_{ST} \approx 140°$, as no more pressure recovery takes place and the base pressure level is reached.

The information from the surface pressure measurement is confirmed by the oil flow visualization image. Fig. 8 shows the observed oil flow pattern on the cylinder at a Reynolds number of Re 5.2×10^5. In order to enable a comparison and ease the visual understanding, the image of the three-dimensional surface of the cylinder was transformed into a two-dimensional image. This also applies for the thermographic images presented below. The distinct green lines in the oil flow visualization correspond to the laminar separation at $\phi_{SL} \approx 102°$ and the turbulent separation at $\phi_{ST} \approx 140°$. The dark line at $\phi \approx 117°$ without any oil-pigment solution left is the angular position of the reattachment of the flow ϕ_R behind the laminar separation bubble. The red vertical line at $90°$ corresponds to a line-laser positioned over the $90°$ pressure tap as a reference. The bright part at the leading edge of the cylinder is due to a reflection of incident daylight in the wind tunnel at the strongly curved surface. The picture was taken 11:30 min after the target Reynolds number was reached. Within the following images, local accumulations at the angular positions of the laminar and the turbulent separation changed the flow field significantly. An inspection of the oil flow pattern after the wind tunnel was stopped showed that the region after the turbulent separation indicates a reversed flow region.
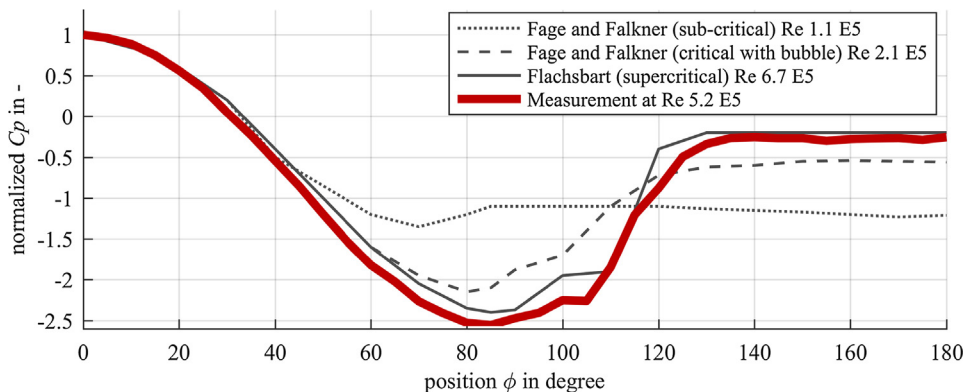

Fig. 7. Normalized surface pressure distributions around a circular cylinder in crossflow for different Reynolds numbers (data from [24]) in comparison with the measured surface pressure distribution around the circular cylinder at Re 5.2×10^5.
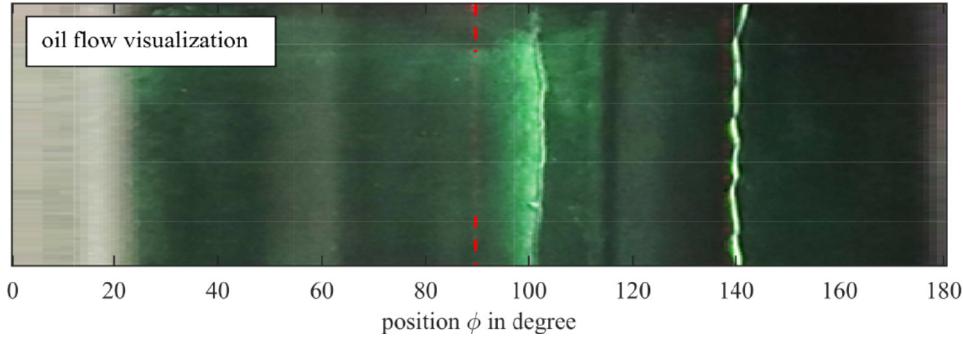
Fig. 8. Oil flow visualization of the flow field around the circular cylinder at Re 5.2×10^5. The distinct green lines correspond to a laminar separation at $\phi_{SL} \approx 102°$ and a turbulent separation at $\phi_{ST} \approx 140°$. The dark line is the reattachment of the flow at $\phi_R \approx 117°$ behind a laminar separation bubble. The red vertical line at 90° corresponds to a line-laser positioned over the 90° pressure tap as a reference. (For interpretation of the references to color in this figure legend, the reader is referred to the web version of this article.)

As an intermediate result the angular positions of the different flow regions accounting to the reference measurements can be itemized as follows:

- Laminar flow: $0° \leqslant \phi \leqslant 101°$
- Laminar separation: $\phi_{SL} \approx 102°$
- Laminar separation bubble: $102° \leqslant \phi \leqslant 116°$
- Reattachment: $\phi_R \approx 117°$
- Turbulent flow: $117° \leqslant \phi \leqslant 139°$
- Turbulent separation: $\phi_{ST} \approx 140°$
- Separated flow: $140° \leqslant \phi \leqslant 180°$

As an indication for the dynamic behavior in the different flow regions, the acoustic measurements, representing the pressure fluctuations on the cylinder's surface, are shown in Fig. 9. The resulting spectrogram shows the magnitude for frequencies of up to 10^4 Hz over the angular position ϕ. The spectrogram is calculated with short time Fourier transforms (STFT) with a window size of 2^{13} values and a Hamming window function. The spectrum in the stagnation point at $\phi = 0°$ can be assumed as the base level with wind tunnel noise as the main signal source. For the following region of laminar flow the rising pressure fluctuations occur at a low frequencies below 200 Hz. The most distinct frequency is at around 156 Hz, which can be explained by the vortex shedding frequency $f_{shedding}$. With the consideration of this frequency, the Strouhal number Sr can be calculated, cf Eq. (3):

$$Sr = \frac{f_{shedding} \, d}{V} \approx 0.5 \tag{3}$$

with the diameter of the cylinder $d = 0.16$ m and the incoming flow speed $V = 50$ m s^{-1}. With an increasing angular position ϕ, the scatter around this frequency grows. The first significant change occurs at the position of the laminar separation at around 102°. Additional
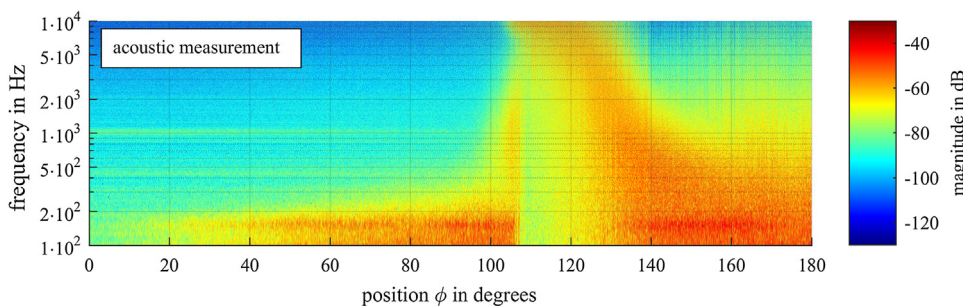
high frequent pressure components lead to a broadband signal. For instance, the magnitude at 500 Hz rises by 10 dB. At $\phi = 107°$, the low and mid-frequency components disappear due to the isolating effect of the laminar separation bubble and the signal consists mainly of high frequency components. The magnitude at 500 Hz decreases by 10 dB and below 200 Hz the magnitude decreases by 20 dB. Within the turbulent boundary layer, the mean frequency of the high frequency components of the signal decrease due to the reduced flow speed in the turbulent boundary layer. For $\phi \geqslant 140°$, the signal passes into a broadband spectrum. As a result, the analysis of the pressure fluctuation shows distinct differences between the different flow regions, which affirms the initial hypothesis.

The next step is to determine the different flow fluctuations by evaluating the temperature fluctuations in the thermographic image series. In Fig. 10 an IR thermographic overview image is depicted with the marked position of the region of interest for the detailed reference and thermographic measurements. The
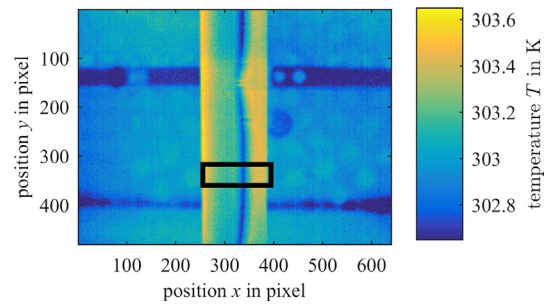

Fig. 10. IR thermographic overview image of the circular cylinder in the test section at Re 5.2×10^5. The black rectangle marks the region of interest for the oil flow and thermographic flow visualization.

Fig. 9. Spectrogram of the acoustic analyses in the boundary layer of the circular cylinder at Re 5.2×10^5 (≈ 50 m s^{-1} windspeed in the test section).

overview image indicates a minor three dimensional effect due to the edges of the different cylinder parts (cf. Section 3.2). For this reason, the chosen region of interest has a reduced dimension in y-direction.

For the comparison with the processed IR thermographic image series, first an IR thermographic image of the cylinder, that is calculated by the arithmetic mean $\overline{T}$ of the image series is shown in Fig. 11. This image represents the initial situation of a single image, with an additional reduction of noise due to the averaging of the image series. For reasons of comparability, the original size of the image is reduced in both dimensions by the factor of 0.5 with a bicubic kernel. This spatial averaging results in a further reduced noise. The resolution of the resulting image is 100×359 pixel. The mean of the IR thermographic images shows regions with different temperature levels. Note that the colder upper left and the colder upper right corners in the image are due to the edges of the used IR-window. Up to $\phi \approx 105°$ the temperature is about 303.15 K. This region corresponds to the laminar flow region with a relatively moderate skin friction. As seen in the oil flow visualization, that region is followed by a laminar separation bubble bounded by the position ϕ_{SL} of the laminar separation and the reattachment of the flow at ϕ_R. This region is characterized by a low temperature due to the reduced heat transfer as a result of the self containment of the laminar separation bubble. Further downstream, the temperature rises due to the higher skin friction in regions with turbulent flow. As the skin friction in the region of separated flow is nearly constant, the temperature reaches a nearly constant level that is overlaid with the reduction of radiation because of the angular dependency of the emission of the cylinder surface. However, the change from turbulent flow to separated flow at $\phi_{ST} \approx 140°$ is very difficult to identify. The shading in the upper left and the upper right corners is due to the limited size of the IR-transmitting windows.

The result of the evaluated IR thermographic image series by means of the temperature temporal standard deviation differs significantly from the previously presented mean of the image series, cf. Fig. 12. The evaluation reveals 5 distinguishable regions that correspond to the different flow regions. In agreement with the acoustic reference measurements, in the region of laminar flow

up to the angular position of $\phi \approx 102°$ the standard deviation of the temperature fluctuations is relatively small due to the flow characteristic of the laminar boundary layer. In the region of the laminar separation bubble, the fluctuations are even smaller. This also agrees with the expectations due to the self containment and isolation within the bubble. The reattachment of the flow at $\phi_R \approx 117°$ results in a high standard deviation, which can be explained on the one hand by the turbulent characteristic of the flow and on the other hand by a slight spatial oscillating movement of the reattachment line within the image series. The region of turbulent flow from $117° \leqslant \phi \leqslant 139°$ is distinguishable by a high standard deviation induced by highly dynamic vortices in the turbulent boundary layer. With the separation at $\phi_{ST} \approx 140°$, the boundary layer separates and the vortex structures expand, which finally results in a lower standard deviation of the temperature fluctuations.

The qualitative result of the evaluation of the Fourier coefficients hardly varies from the ones evaluated with the standard deviation, cf. Fig. 13. The qualitative information in the resulting images is equal, because different temperature fluctuations due to different flow regions are visualized.

In contrast to the original single thermographic image respectively the mean temperature $\overline{T}$ of the image series, a distinction between the turbulent and the separated flow is possible even in situations with a low thermal contrast between the measurement object and the incoming flow. This fact is depicted in Fig. 14. The data points represent the normalized (in the range between the minimum and maximum value of each measure) arithmetic means for 500 pixels within the different flow regions and the error bars visualize the corresponding measurement uncertainties with a coverage factor of 3. As a result, the evaluation of a time series enhances the separability between the turbulent and the separated region. Between the evaluation with the standard deviation and the Fourier coefficients, no significant difference is observed. In order to quantify the differences between both evaluation methods, a comparison in terms of the contrast to noise ratio (CNR) between each pairing of different flow regions is presented. The CNR is determined for the different flow regions a and b by
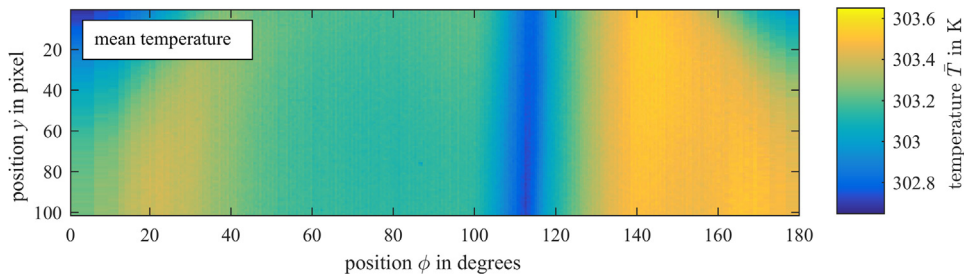

Fig. 11. Mean of the IR thermographic image series of the circular cylinder at Re 5.2×10^5 (≈ 50 m s^{-1} wind speed in the test section).
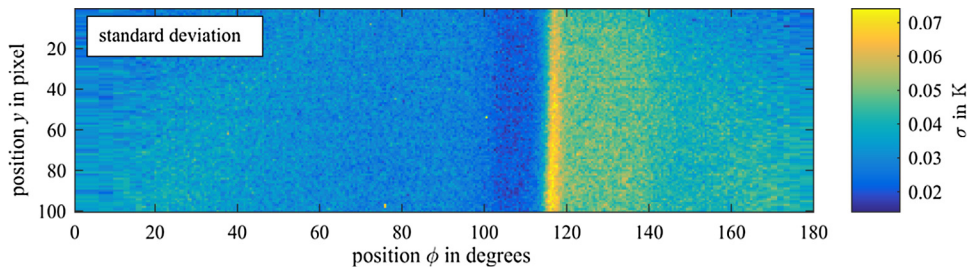

Fig. 12. Processed IR thermographic image series of the circular cylinder at Re 5.2×10^5 by means of the temporal arithmetic standard deviation σ.
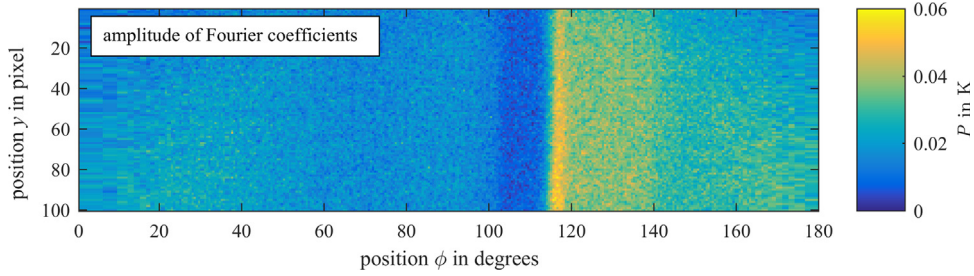
Fig. 13. Processed IR thermographic image series of the circular cylinder at Re 5.2×10^5 by means of the amplitude P of selected Fourier coefficients of the time series.
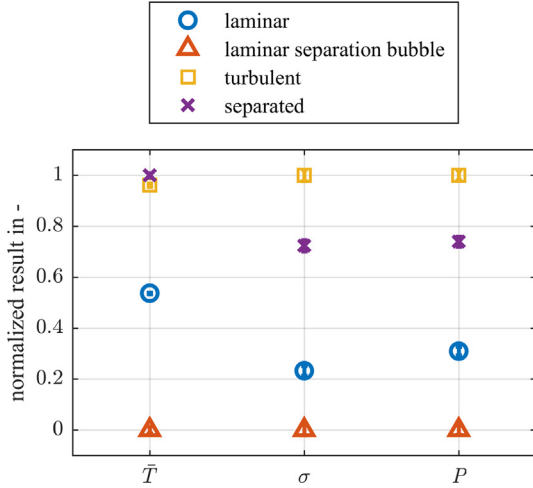

Fig. 14. Comparison of the mean temperature $\overline{T}$ of the thermographic image series with the results of the presented evaluation methods. The data points represent the normalized arithmetic means within the different flow regions and the error bars the measurement uncertainty with a coverage factor of 3.

Table 1
Comparison of the contrast to noise ratios (CNR) for the two presented evaluation methods using σ and P, respectively.

Pair of flow conditions	CNR_σ	CNR_P	Improvement
Laminar – laminar separated	1.273	2.846	123.5 %
Laminar – turbulent	12.651	12.976	2.6 %
Laminar – separated	5.254	4.658	−11.3 %
Laminar separated – separated	11.378	13.718	20.6 %
Laminar separated – turbulent	19.769	25.603	29.5 %
Turbulent – separated	1.400	1.563	11.6 %

$$CNR_{a-b} = \frac{\left(\overline{T}_a - \overline{T}_b\right)^2}{s_a^2 + s_b^2}. \tag{4}$$

In this equation $\overline{T}$ is the spatial arithmetic mean of the 500 pixels within the flow regions and s the corresponding spatial standard deviation. The results are given in Table 1. The comparison shows that, except for the difference between the laminar and the separated flow condition, the CNR for the Fourier analysis is higher than the CNR for the evaluation of the temperature standard deviation. Even though the CNR between the turbulent and the separated flow condition is relatively small, an enhancement of 11.6 % can be achieved with an evaluation by a Fourier analysis.

4.2. NACA 63₃-618

For the measurements on the NACA $63_3 - 618$ airfoil, an exemplary image set of the suction side at an angle of attack of 12
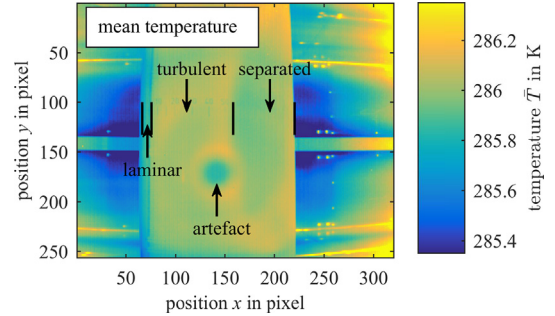

Fig. 15. Mean of the IR thermographic image series of the NACA 63₃-618 airfoil in the test section at Re 2.0×10^6.

degrees is presented. At this angle of attack, the airfoil is stalled and a trailing edge separation is expected. The mean of the IR thermographic image series of the airfoil in the wind tunnel at a Reynolds number of Re 2.0×10^6 is depicted in Fig. 15. The spatial resolution of the result corresponds to the full-frame resolution of the IR thermographic camera with 640×512 pixels. The resulting image is not corrected in terms of optical and geometrical distortions. The laminar turbulent transition is located near the leading edge, where the temperature on the surface increases from 285.85 to 286.02 K ($\Delta T \approx 0.17$ K). The cold circular spot in the middle of the image is an artefact due to a reflection of the cooled sensor array in the IR transmitting window. Towards the trailing edge a separation region (stall cell) can be observed, indicated by a small drop in temperature. Due to the limited span of the airfoil, the stall cell is bent towards the bottom and the top of the wind tunnel test section. Compared to the laminar turbulent transition the temperature difference between turbulent flow with 286.02 K and separated flow with 285.93 K is relatively small ($\Delta T \approx 0.09$ K). The result of the evaluation of an image series in terms of temperature fluctuations shows a more significant distribution under the same conditions, even though the absolute difference is smaller, cf. Fig. 16. The more homogeneous and less disturbed regions enable a thermographic flow visualization in terms of a visual interpretation and distinction of the different flow regions. The time resolved image series is evaluated by the described method for selected Fourier coefficient described in Section 2. The increase of temperature fluctuations in the region of turbulent flow allows to distinguish between laminar and turbulent flow ($\Delta P \approx 0.0125$ K) as well as turbulent and separated flow ($\Delta P \approx 0.0113$ K). Even though the localization of the separated flow region is already possible in the image that is averaged over the image series, the evaluated image shows the temperature fluctuations in the boundary layer and therefore supports the initial hypothesis of temperature fluctuations that are resolvable by the image processing. A secondary positive effect of the evaluation is that steady artefacts such as the reflection of the cooled sensor array do not have an impact on
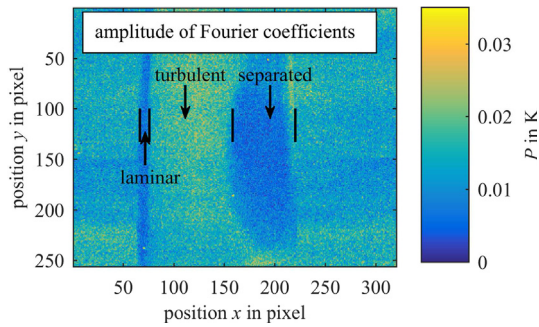
Fig. 16. Evaluated thermographic image series of the NACA 63_3-618 airfoil in the test section at Re 2.0×10^6.

the result. However, a distinction between the laminar and the separated flow condition is still difficult, which agrees with the measurement results at the cylinder, cf. Table 1. A priori knowledge about the flow structure is required for identifying the stall cell at the trailing edge of the airfoil.

5. Conclusion and outlook

A method has been demonstrated in which the evaluation of a thermographic image series goes beyond displaying the laminar-turbulent transition with a single image respectively the mean of an image series on a non-heated measurement object. Regions that are characterized by differences in their flow induced temperature fluctuations, such as separated flow regions, are revealed by time-resolved IR thermography. In contrast to the visualization with a single thermographic image or the arithmetic mean of an thermographic image series, the evaluation of temperature fluctuations by means of a temporal standard deviation or by selected Fourier coefficients enables a distinction between turbulent and separated flow regions, even in conditions without explicit additional external heating of the measurement object. The presented method can be used accompanying the established thermographic flow visualization methods to increase the obtained information in terms of a distinction between turbulent and separated flow regions. The flow visualization method was successfully validated by conventional measurement techniques such as mean surface pressure measurements, oil-flow visualization and an acoustic evaluation of the boundary layer pressure fluctuation in a wind tunnel experiment. In contrast to the established methods the demonstrated approach enables a very fast and absolutely non-invasive way to visualize separated flow regions with no preparation of the rotor blade. These features are both useful in wind tunnel tests to evaluate stall and the extent of 2D flow conditions, as well as in field measurements to assess the real operating conditions of wind turbines in operation. The obtained flow information enable the identification of problem zones and can be used for the positioning of flow control add-ons in order to avoid undesired flow separation. Future investigations for the improvement of the evaluation will focus on an additional spatial evaluation in the different flow regions. After the successful demonstration of the method in the wind tunnel, the transfer to measurements on wind turbines in standstill and in operation will be investigated next.

Conflict of interest

The authors declare that there are no conflicts of interest.

References

[1] E. Achenbach, Influence of surface roughness on the cross-flow around a circular cylinder, J. Fluid Mech. 46 (1971) 321–335, https://doi.org/10.1017/s0022112071000569.

[2] P. Bæk, P. Fuglsang, Experimental detection of transition on wind turbine airfoils, in: Proceedings of the European Wind Energy Conference and Exhibition, 2009, pp. 1628–1652.

[3] G.P. Corten, Flow separation on wind turbines blades Ph.D. thesis. Dissertation, Utrecht University, 2001.

[4] B.K. Crawford, G.T. Duncan, D.E. West, W.S. Saric, Quantitative boundary-layer transition measurements using IR thermography, AIAA SciTech (2014) 13–17, https://doi.org/10.2514/6.2014-1411.

[5] B.K. Crawford, G.T. Duncan, D.E. West, W.S. Saric, Robust, automated processing of ir thermography for quantitative boundary-layer transition measurements, Exp. Fluids 56 (2015) 149, https://doi.org/10.1007/s00348-015-2011-x.

[6] C. Dollinger, N. Balaresque, M. Sorg, Thermographic boundary layer visualisation of wind turbine rotorblades in operation, in: EWEA Europe's Premier Wind Energy Event, Barcelona, 2014.

[7] C. Dollinger, N. Balaresque, M. Sorg, G. Goch, Thermographic measurement method for turbulence boundary layer analysis on wind turbine airfoils, in: AWEA Wind Power Conference and Exhibition, Las Vegas, 2014.

[8] A.D. Gardner, C.C. Wolf, M. Raffel, A new method of dynamic and static stall detection using infrared thermography, Exp. Fluids 57 (2016) 149, https://doi.org/10.1007/s00348-016-2235-4.

[9] E. Gartenberg, W.G. Johnson, R.E. Wright, D.L. Carraway, C.B. Johnson, Boundary-layer transition-detection in a cryogenic wind tunnel using infrared imaging, AIAA J. 30 (1992) 444–446, https://doi.org/10.2514/3.10936.

[10] E. Gartenberg, A.S. Roberts, Airfoil transition and separation studies using an infrared imaging system, J. Aircraft 28 (1991) 225–230, https://doi.org/10.2514/3.46016.

[11] R. Gasch, J. Twele, Wind Power Plants, Springer Nature, 2012, https://doi.org/10.1007/978-3-642-22938-1.

[12] M.G. el Hak, D.M. Bushnell, Separation control: Review, J. Fluids Eng. 113 (1991) 5–30, https://doi.org/10.1115/1.2926497.

[13] M.O. Hansen, Aerodynamics of Wind Turbines, Earthscan, London, 2008.

[14] E. Hau, Wind Turbines: Fundamentals, Technologies, Application, Economics, Springer Nature, 2013, https://doi.org/10.1007/978-3-642-27151-9.

[15] J.T. Heineck, E. Schülein, M. Raffel, Boundary layer transition detection on a rotor blade using rotating mirror thermography, in: 5th American Helicopter Society Decenial Specialist Meeting, Aeromechanics, San Francisco, 2014.

[16] W.H. Hucho, Aerodynamics of Road Vehicles: From Fluid Mechanics to Vehicle Engineering, Elsevier Science, 2013.

[17] L.A. Joseph, A. Borgoltz, W. Devenport, Infrared thermography for detection of laminar-turbulent transition in low-speed wind tunnel testing, Exp. Fluids 57 (2016) 77, https://doi.org/10.1007/s00348-016-2162-4.

[18] W. Lang, A.D. Gardner, S. Mariappan, C. Klein, M. Raffel, Boundary-layer transition on a rotor blade measured by temperature-sensitive paint, thermal imaging and image derotation, Exp. Fluids 56 (2015) 118, https://doi.org/10.1007/s00348-015-1988-5.

[19] L. de Luca, G.M. Carlomagno, G. Buresti, Boundary layer diagnostics by means of an infrared scanning radiometer, Exp. Fluids 9 (1990) 121–128, https://doi.org/10.1007/BF00187411.

[20] L. de Luca, G. Guglieri, G. Cardone, G.M. Carlomagno, Experimental analysis of surface flow on a delta wing by infrared thermography, AIAA J. 33 (1995) 1510–1512, https://doi.org/10.2514/3.12574.

[21] P. Medina, S. Schreck, J. Johansen, L. Fingersh, Oil-flow visualization on a swt-2.3-101 wind turbine, in: 29th AIAA Applied Aerodynamics Conference, American Institute of Aeronautics and Astronautics (AIAA), 2011, https://doi.org/10.2514/6.2011-3818.

[22] A.B. Meinel, M.P. Meinel, Applied solar energy. An introduction. Addison-Wesley series in physics. 2. printing ed., Addison-Wesley Publ., Reading, 1977.

[23] S. Montelpare, R. Ricci, A thermographic method to evaluate the local boundary layer separation phenomena on aerodynamic bodies operating at low reynolds number, Int. J. Therm. Sci. 43 (2004) 315–329, https://doi.org/10.1016/j.ijthermalsci.2003.07.006.

[24] M. Morkovin, Flow around circular cylinder–a kaleidoscope of challenging fluid phenomena, in: ASME Symposium on Fully Separated Flows, 1964, pp. 102–118.

[25] T. Muneer, Solar Radiation and Daylight Models, Routledge, London, 2004.

[26] A. Pellegrino, C. Meskell, Vortex shedding from a wind turbine blade section at high angles of attack, J. Wind Eng. Ind. Aerodyn. 121 (2013) 131–137, https://doi.org/10.1016/j.jweia.2013.08.002.

[27] A. Quast, Detection of transition by infrared image techniques, in: 12th International Congress on Instrumentation in Aerospace Simulation Facilities (ICIASF 87), Williamsburg, 1987.

[28] M. Raffel, C.B. Merz, T. Schwermer, K. Richter, Differential infrared thermography for boundary layer transition detection on pitching rotor blade models, Exp. Fluids 56 (2015) 30, https://doi.org/10.1007/s00348-015-1905-y.

[29] R. Ricci, S. Montelpare, A quantitative ir thermographic method to study the laminar separation bubble phenomenon, Int. J. Therm. Sci. 44 (2005) 709–719, https://doi.org/10.1016/j.ijthermalsci.2005.02.013.

[30] K. Richter, E. Schülein, Boundary-layer transition measurements on hovering helicopter rotors by infrared thermography, Exp. Fluids 55 (2014) 1755, https://doi.org/10.1007/s00348-014-1755-z.

[31] H. Schlichting, Boundary-layer theory, 7 ed., McGraw-Hill series in mechanical engineering, McGraw-Hill, New York, 1979.

[32] B. Simon, A. Filius, C. Tropea, S. Grundmann, IR thermography for dynamic detection of laminar-turbulent transition, Exp. Fluids 57 (2016) 93, https://doi.org/10.1007/s00348-016-2178-9.

[33] S. Vey, H.M. Lang, C.N. Nayeri, C.O. Paschereit, G. Pechlivanoglou, Extracting quantitative data from tuft flow visualizations on utility scale wind turbines, J. Phys: Conf. Ser. 524 (2014) 012011, https://doi.org/10.1088/1742-6596/524/1/012011.